PCCP

PAPER

View Article Online
View Journal | View Issue

Cite this: *Phys. Chem. Chem. Phys.*, 2020, **22**, 17833

Thermal transport properties of novel two-dimensional CSe†

Bing Lv,[ab] Xiaona Hu,[c] Xuefei Liu,[ab] Zhaofu Zhang,[d] Jia Song,[e] Zijiang Luo[f] and Zhibin Gao*[g]

Received 29th April 2020,
Accepted 16th July 2020

DOI: 10.1039/d0cp02298e

rsc.li/pccp

Recently, as a novel member of the IV–VI group compounds, two-dimensional (2D) buckled monolayer CSe has been discovered for use in high-performance light-emitting devices (Q. Zhang, Y. Feng, X. Chen, W. Zhang, L. Wu and Y. Wang, *Nanomaterials*, 2019, **9**, 598). However, to date, the heat transport properties of this novel CSe is still lacking, which would hinder its potential application in electronic devices and thermoelectric materials that can generate electricity from waste heat. Here we systematically study the heat transport properties of monolayer CSe based on *ab initio* calculations and phonon Boltzmann transport theory. We find that the lattice thermal conductivity κ_{lat} of monolayer CSe is around 42 W m^{-1} K^{-1} at room temperature, which is much lower than those of black phosphorene, buckled phosphorene, MoS_2, and buckled arsenene. Moreover, the longitudinal acoustic phonon mode contributes the most to the κ_{lat}, which is much larger than those of the out-of-plane phonon mode and transverse acoustic branches. The calculated size-dependent κ_{lat} shows that the sample size can significantly reduce the κ_{lat} of monolayer CSe and can persist up to 10 μm. These discoveries provide new insight into the size-dependent thermal transport in nanomaterials and guide the design of CSe-based low-dimensional quantum devices, such as thermoelectric devices.

1 Introduction

The thermal energy is a crucial issue for electricity generation owing to the needs of fundamental science and practical applications since over 90% of our energy consumption and utilization involves heat. Due to the quantum confinement effect, the thermal transport in nanomaterials is quite different from that in their bulk counterpart.[2,3] Thermoelectric materials, which can generate electricity from waste heat, could play a pivotal role in mitigating the sustainability challenge. The conversion efficiency of thermoelectric materials is measured by their figure of merit ZT, written as $ZT = S^2\sigma T/(\kappa_e + \kappa_{lat})$, in which S, σ, T, κ_e and κ_{lat} are the Seebeck coefficient, electrical conductivity, absolute temperature, electronic thermal conductivity and lattice thermal conductivity, respectively. Because of the contradictory relationship between S and σ, κ_{lat} becomes a relatively independent factor in ZT.[4] Minimizing κ_{lat} is very important for thermoelectrics to efficiently convert unavoidable waste heat to electricity, because the figure of merit ZT is inversely proportional to κ_{lat}.[4,5] Furthermore, in semiconductors and insulators, most of the heat is carried by the phonons. In contrast, the electronic contribution to thermal conductivity is almost negligible.[5–8] Therefore, seeking materials with small κ_{lat} is of great significance in the thermoelectric community to search for an ideal material with high thermoelectric performance.[4,9,10]

Two-dimensional (2D) semiconducting blue phosphorus[11,12] have attracted much attention owing to its superior electronic applications. Materials with the same number of outermost electrons usually exhibit similar physical and chemical properties. Therefore, isoelectronic counterparts of blue phosphorene in the IV–VI group have shown much gravitation, such as β-GeSe for Na-ion batteries,[13] SiS, and SiSe as anode materials for Na/K-ion batteries.[14]

In 2019, a novel monolayer CSe with high-performance photovoltaic properties was predicted,[1] which possesses a wide indirect band gap sensitive to the in-plane strain. Recently, the dynamic stability of monolayer α-CSe was confirmed by calculating the phonon spectra using density functional perturbation theory.[18] Besides, the previous result showed that

[a] *School of Physics and Electronic Science, Guizhou Normal University, Guiyang 550025, China*
[b] *Key Laboratory of Low Dimensional Condensed Matter Physics of Higher Educational Institution of Guizhou Province, Guizhou Normal University, Guiyang 550025, China*
[c] *School of Biological Sciences, Guizhou Education University, Guiyang 550018, China*
[d] *Department of Engineering, Cambridge University, Cambridge, CB2 1PZ, UK*
[e] *Shanghai Engineering Research Center of 3D Printing Materials, Shanghai Research Institute of Materials, Shanghai 200437, China*
[f] *School of Information, Guizhou University of Finance and Economics, Guiyang 550025, China*
[g] *Department of Physics, National University of Singapore, Singapore, 117551, Republic of Singapore. E-mail: zhibin.gao@nus.edu.sg*

† Electronic supplementary information (ESI) available. See DOI: 10.1039/d0cp02298e

β-phosphorene possesses a smaller κ_{lat} compared with α-phosphorene.[17] What's more, β-SnSe also has the lowest lattice thermal conductivity κ_{lat} compared with α-, γ-, δ-, and ε-SnSe.[19] Moreover, the structure of novel monolayer CSe is the same as β-SnSe. These facts motivate us to speculate that the thermal conductivity of monolayer CSe is also low. In addition, is the thermal conductivity of monolayer CSe lower than that of blue phosphorene? The answer deserves to be explored. Besides, the thermal transport properties of monolayer CSe are still lacking, which has potential applications for electricity generation and in optoelectronic devices. In this study, the phonon transport properties of monolayer CSe are systematically investigated based on first-principles calculations and phonon Peierls–Boltzmann equation. These methods have been successfully used in 2D and 3D materials.[4,17,20–27] For example, Gajaria *et al.* showed that the theoretical thermoelectric properties of GaX (X = P, As, Sb) agree well with the experimental results.[25] Additionally, Kagdada *et al.* proved that GeTe in the rhombohedral phase exhibits high thermoelectric performance as well.[26] Previous work has further proved that strong anharmonicity would lead to a lower lattice thermal conductivity in the GeTe monolayer by solving the phonon Boltzmann transport equation (PBTE).[27] We find that monolayer CSe has a low κ_{lat} of 42 W m^{-1} K^{-1} at room temperature, which is much lower than that of buckled monolayer phosphorene (108.8 W m^{-1} K^{-1},[17] 106.6 W m^{-1} K^{-1}[21] and 569.7 W K^{-1}[23]), monolayer arsenene (65.4 W m^{-1} K^{-1}[17] and 183.0 W K^{-1}[21]), and slightly higher than those of monolayer silicene (28.6 W m^{-1} K^{-1}[20]) and monolayer borophene (14.34 W m^{-1} K^{-1}[28]). Moreover, the size effect in low-dimensional materials plays a more important role than in bulk materials.[4] Our results show that the κ_{lat} of monolayer CSe can be further suppressed from 42 W m^{-1} K^{-1} to 29 W m^{-1} K^{-1} when the sample length L decreases from 10 μm to 100 nm at 300 K.

2 Results and discussion

Fig. 1(a) and (b) show the equilibrium atomic structure of monolayer CSe with buckling. This atomic configuration is identical to that of blue phosphorus.[11] The structure can be achieved using the C–Se bond instead of the P–P bond in blue phosphorus. Since blue phosphorus has been successfully grown in experiments,[12] monolayer CSe would have great potential with the same experimental techniques and crystal structure. For comparison, the optimized lattice parameters are shown in Table 1. Our calculated lattice constants are $a_1 = a_2 =$ 3.05 Å and the bond length is 2.05 Å, which are in good agreement with the previous studies.[1,11,17] Besides, the lattice constant and bond length of CSe is smaller than those of blue phosphorus, indicating a stronger atomic interaction. However, the bond angle is slightly larger than that of blue phosphorus. Furthermore, the bulking thickness is much smaller than that of blue phosphorus, indicating lower energy of monolayer CSe. In contrast to blue phosphorus monolayer, buckling distance d and effective thickness h of CSe monolayer are reduced to 1.04 Å and 4.64 Å.

In order to verify the stability of monolayer CSe, we calculate the phonon dispersion along high-symmetry points, as shown in Fig. 1(c). It is free from imaginary frequency, indicating the dynamical stability of monolayer CSe. Obviously, there is a frequency gap between acoustic phonons and optical phonons ranging from 235 cm^{-1} to 375 cm^{-1}. This acoustic–optical phonon (a–o) gap originates from the difference between the mass of Se and C elements. Since the phonon–phonon scattering must satisfy energy conservation, the A + A ↔ O (A and O stand the acoustic and optical phonons) scattering channels can be significantly suppressed by this large a–o gap, which will have an effect on the thermal transport properties of monolayer CSe. Usually, a larger a–o frequency gap could lead to a higher lattice thermal conductivity.[29] The calculated

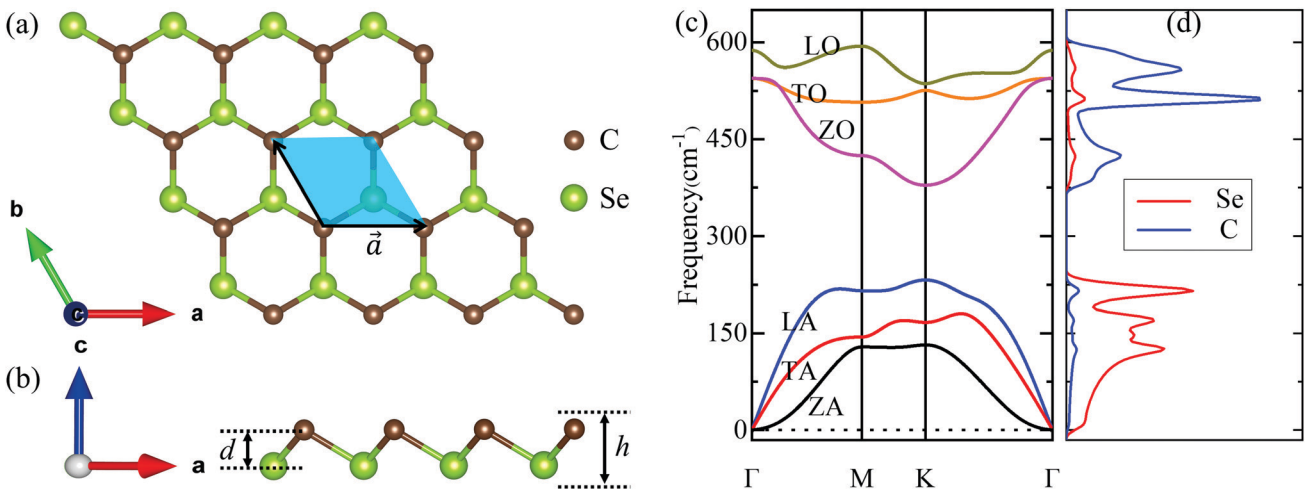

Fig. 1 (a) Top and (b) side view of the optimized structure of monolayer CSe in a 3 × 3 supercell. (c) Phonon dispersion curves along the high-symmetry points. The phonon branches (ZA, TA, LA, ZO, TO and LO) are indicated in black, red, blue, magenta, orange and dark yellow, respectively. (d) The phonon partial densities of states of monolayer CSe. The unit cell is marked by blue shading in (a). $\vec{a}$ is the corresponding lattice vectors and d is the buckling distance. The effective thickness h is defined as the summation of d and two van der Waals radii of the outermost surface atom of the structure.[15,16]

Table 1 The optimized structural parameters of CSe and blue phosphorene monolayers. Other available values reported in literature are also given

Materials	Lattice constants (Å)	Bond length (Å)	Bond angle (°)	d (Å)	h (Å)
β-CSe	3.05, 3.065[a]	2.05, 2.055[a]	96.28, 96.45[a]	1.04, 1.044[a]	4.64
Blue-P	3.27, 3.28[a], 3.28[b], 3.326[c]	2.26, 2.261[a], 2.27[c]	92.91, 92.907[a]	1.23, 1.238[b]	5.13

[a] Ref. 1. [b] Ref. 17. [c] Ref. 11.

phonon partial densities of states (DOS) of monolayer CSe are shown in Fig. 1(d), there are some very small negative frequencies due to frequency broadening and can be ignored. This broadening is a setting of the Gaussian integral that is a conventional algorithm in the first-principles calculations. We find that the vibrations of selenium (Se) atoms mainly contribute to the DOS of the three acoustic phonon modes of longitudinal acoustic LA, transverse acoustic TA, and out-of-plane flexible ZA modes, while the vibrations of carbon (C) atoms almost dominate the DOS of the optical phonon branches of transverse optical TO, longitudinal optical LO, and out-of-plane flexural optical ZO phonon modes.

According to the $\kappa \times p$ theory of phonon, the phonon branches of monolayer CSe can be sorted according to the continuity of their eigenvectors[22,30,31]

$$|\Sigma e_{k,\sigma_1}{}^*(i)\cdot e_{k+\Delta,\sigma_2}(i)| = |\delta_{\sigma_1,\sigma_2} - o(\Delta)|, \quad (1)$$

in which $e_{k,\sigma}{}^*(i)$ is the displacement of the atomic index i in a phonon vibrational mode (k,σ). Δ is small variation of wave vector. Fig. 2(a) and (b) present the vibrations of Se and C atoms in the xy plane and z direction. This result is in a good agreement with the image shown in Fig. 1(d). Furthermore, there is a certain degree of hybridization between the vibrations of Se (xy) atoms and C (xy) atoms. What's more, the TO and LO optical branches mainly are derived from the xy plane vibrations of the C atoms, while the ZO optical phonon mode originates from the z direction vibrations of the C atoms. Similarly, the vibrations of Se atoms in the xy plane contribute the most to the TA and LA acoustic phonon branches and the vibrations along the z axis almost lead to the ZA acoustic phonon branch.

According to the phonon Boltzmann transport theory, the lattice thermal conductivity κ_{lat} can be expressed as[32]

$$\kappa_{\alpha\beta} = \frac{1}{V}\sum_{\lambda} C_{\lambda}\nu_{\lambda\alpha}\nu_{\lambda\beta}\tau_{\lambda}, \quad (2)$$

where V is the volume of the primitive cell. C_{λ}, τ_{λ}, and $\nu_{\lambda\alpha}$ are the specific heat, phonon relaxation time, and phonon group velocity along with the cartesian direction α of each single phonon mode $\lambda(\nu, \mathbf{q})$, respectively. For 2D materials, thickness is a necessary parameter for the calculation of κ_{lat}. The calculated κ_{lat} should be normalized by multiplying by L_z/h, as L_z and h are the length of the primitive cell along the z direction and the effective thickness of the 2D material, respectively. In this work, the effective h is 4.64 Å, as shown in Table 1 for monolayer CSe.

The calculated κ_{lat} of monolayer CSe is plotted in Fig. 3(a) based on the iterative approach of the phonon Boltzmann transport equation. For comparison, we also show the result of the single mode relaxation time approximation (RTA) solution. It is clearly found that the RTA method severely underestimates the κ_{lat} compared with the iterative approach.[33] The room-temperature κ_{lat} is 42 W m^{-1} K^{-1}, by the iterative approach,

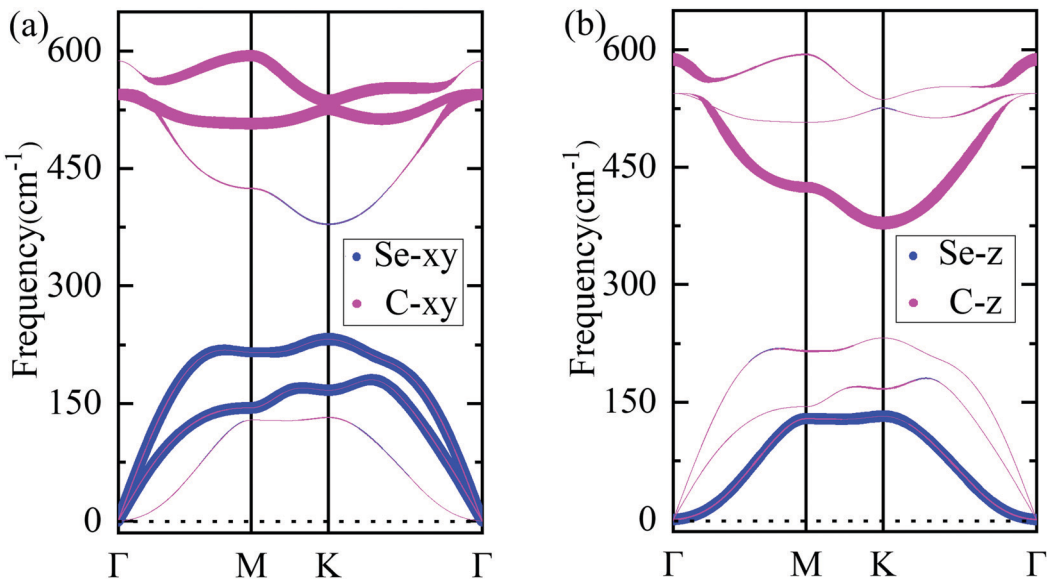

Fig. 2 (a) Orbital-resolved phonon spectra showing in-plane xy vibrations of Se and C atoms. (b) Orbital-resolved phonon spectra showing in-plane z vibrations of Se and C atoms. The plane xy and z vibrations of Se atoms are indicated in blue. The plane xy and z vibrations of C atoms are indicated in magenta.

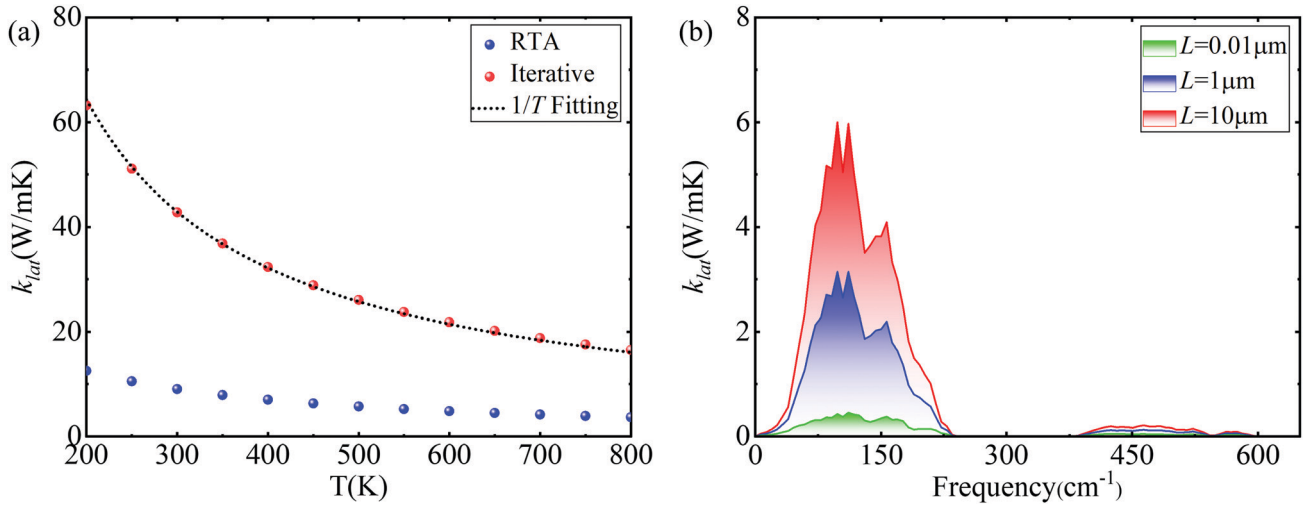

Fig. 3 (a) Lattice thermal conductivity of monolayer CSe as a function of temperature. The black dashed curve represents the $\sim 1/T$ fitting to the temperature dependent κ_{lat}. T represents the temperature. (b) Frequency distribution of κ_{lat} at 300 K for L = 0.01 μm, 1 μm and 10 μm. L represents the sample size. The results of L = 0.01 μm, 1 μm and 10 μm are indicated in gradient colors with green and white, blue and white, red and white, respectively.

which is much larger than that of 9 W m^{-1} K^{-1} in the RTA solution. When temperature increases, the phonon–phonon scattering increases, and the Umklapp scattering gradually dominates the phonon transport behavior.[4,10] Therefore, the κ_{lat} decreases with temperature from 200 K to 800 K. We find that the κ_{lat} of monolayer CSe can be nicely fitted by a function of $\kappa_{lat} \propto 1/T$, T refers to the temperature, which indicates the dominant role of the Umklapp scattering in determining the heat transport properties of monolayer CSe. In 2D materials, the κ_{lat} of monolayer CSe is much lower than those of graphene (3716.6 W m^{-1} K^{-1}),[21] nitrogene (763.4 W m^{-1} K^{-1}),[21] black phosphorene (83.5 W m^{-1} K^{-1}),[34] buckled phosphorene (108.8 W m^{-1} K^{-1}),[17] MoS_2 (84 ± 17 W m^{-1} K^{-1}),[35] buckled arsenene (65.4 W m^{-1} K^{-1}),[17] and WSe_2 (53 W m^{-1} K^{-1}).[36] The frequency dependent κ_{lat} at room temperature is shown in Fig. 3(b) with different sample sizes L. It is found that low-frequency phonons contribute the most of the κ_{lat} of monolayer CSe, which is almost derived from the ZA, TA, and LA acoustic phonons. Moreover, this trend of the contribution becomes more and more weaker with the reduction of the sample size. This phenomenon is caused due to the effect of boundary scattering. When the sample length decreases, the boundary scattering gradually becomes dominant compared with the intrinsic phonon–phonon scattering. In this situation, the κ_{lat} for monolayer CSe contributed from optical phonon modes is negligible compared with the acoustic phonons, as shown in Fig. 3(b).

According to eqn (2), the κ_{lat} is a crucial parameter and proportional to the phonon velocity that is defined as $\vec{v} = d\omega/d\vec{q}$. Due to the dominant role of acoustic phonons in monolayer CSe, we plot the phonon group velocity of acoustic phonon modes in Fig. 4(a). Specifically, the maximum group velocities of ZA, TA, and LA acoustic phonons are 3.28 × 10^3 m s^{-1}, 4.69 × 10^3 m s^{-1}, and 7.22 × 10^3 m s^{-1}, respectively. The group velocity of LA acoustic phonons is around two times higher than that of the ZA acoustic phonons. This will lead to a large mode contribution of LA acoustic phonons compared with other two acoustic phonons, which has been verified in Fig. 4(d) for monolayer CSe materials.

Three-phonon scattering phase space (W) is a very important factor to understand the heat transport properties of nanomaterials. It is a quantitative measurement of the total space available for the three-phonon process allowed by the conservation of energy. A large W indicates that more space is available for the three-phonon scattering processes.[23] Therefore, it is a good indicator of small phonon lifetime and κ_{lat}. Fig. 4(b) shows the scattering phase space W of the ZA, TA, and LA acoustic phonon modes in monolayer CSe. The scattering phase space gradually decreases with increasing phonon frequency of all acoustic phonon modes and the ZA phonon branch possesses a relatively larger W compared with TA and LA acoustic modes. As we mentioned above, there is a large a–o gap in monolayer CSe, which will suppress the number of A + A ↔ O scattering channels. Moreover, the W of ZA, TA and LA acoustic branches slightly increase at high frequencies. A big jump in the ZA mode is observed at around 140 cm^{-1}, indicating more involved scattering channels such as ZA + ZA ↔ ZA, ZA + TA ↔ TA, and ZA + LA ↔ LA.[21,37]

Based on eqn (2), except for the phonon group velocity and scattering phase space, phonon relaxation time is another crucial factor that determines the κ_{lat}. It is not only determined by the scattering strength, but also by the total number of phonon–phonon scattering. The intrinsic anharmonic phonon lifetime as a function of frequency at 300 K with mode resolution is shown in Fig. 4(c). The ZA branch has a smaller phonon lifetime owing to the large scattering phase space shown in Fig. 4(b). However, LA acoustic phonon possesses a large phonon lifetime due to the small scattering channels. Our results are similar to those of reported works of buckled β-NAs and monolayer β-NSb.[23]

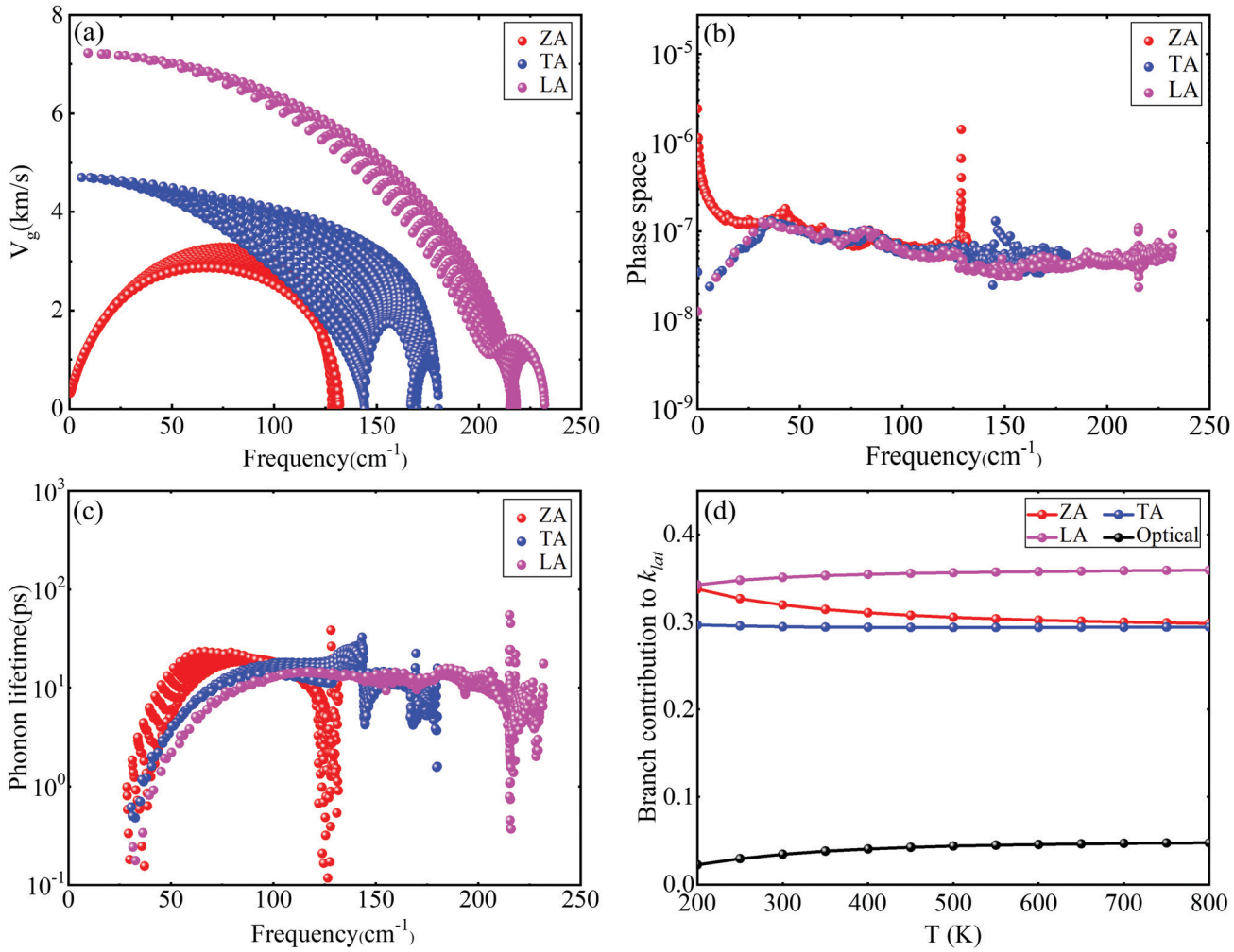

Fig. 4 (a) The phonon group velocity of ZA, TA and LA acoustic phonon branches at 300 K. (b) Three-phonon scattering phase space of ZA, TA and LA acoustic phonon branches at 300 K. (c) The phonon lifetime of ZA, TA and LA acoustic phonon branches at 300 K. (d) The relative contribution (percentage) with phonon mode resolution. The results of acoustic phonon branches (ZA, TA and LA) and optical phonon modes are indicated in red, blue, magenta and black, respectively.

The mode contribution (percentage) to the total κ_{lat} at 300 K is shown in Fig. 4(d). It is found that the ZA, TA and LA acoustic branches play the dominant role in the lattice thermal conductivity of monolayer CSe. Among these, the LA acoustic mode contributes a larger percentage than the ZA, TA, and optical phonon modes. This is similar to the physical picture observed in other 2D transition metal dichalcogenides (TMDs).[20,36] In contrast, the remaining three optical phonon branches play a minor role in the heat transport properties of monolayer CSe. Specifically, at room temperature, the percentage contribution of the ZA, TA, LA acoustic branches, and the sum of contributions of optical branches to the total κ_{lat} are 31.9%, 29.5%, and 35.1% and 3.50%, respectively. Furthermore, these percentages are almost unsensitive to temperature. It is found that the contribution of the TA and LA acoustic branches remain almost unchanged, while that of the ZA acoustic branch decreases slowly. In 2D buckling materials, it breaks the reflection symmetry, which will enhance the phonon–phonon scattering phase space of the ZA acoustic branch.[21]

According to the Slack model, long-wave (acoustic) phonons are the main carrier for heat transport.[38] Generally, a small Debye temperatures Θ_D means a small κ_{lat}.[39] The definition of Θ_D is expressed as $\Theta_D = h\omega_{max}/k_B$, in which ω_{max} is the maximum frequency of the acoustic phonon branches and k_B is the Boltzmann constant of 1.381×10^{-23} J K^{-1}. The calculated Θ_{ZA}, Θ_{TA} and Θ_{LA} are 30.21 K, 41.27 K and 53.13 K, respectively. Θ_{LA} is the largest and contributes the most to the κ_{lat} of monolayer CSe. This is well consistent with the phonon relaxation time shown in Fig. 4(c) and mode contribution in Fig. 4(d).

The intensity of each phonon–phonon scattering can be reflected by the mode-dependent Grüneisen parameter γ which is defined as[40]

$$\gamma = -\frac{d \ln \omega}{d \ln V}, \quad (3)$$

The calculated mode-dependent γ of monolayer CSe is shown in Fig. 5(a). γ indicates the anharmonic strength and a large γ means a large phonon anharmonicity. It is clear that the

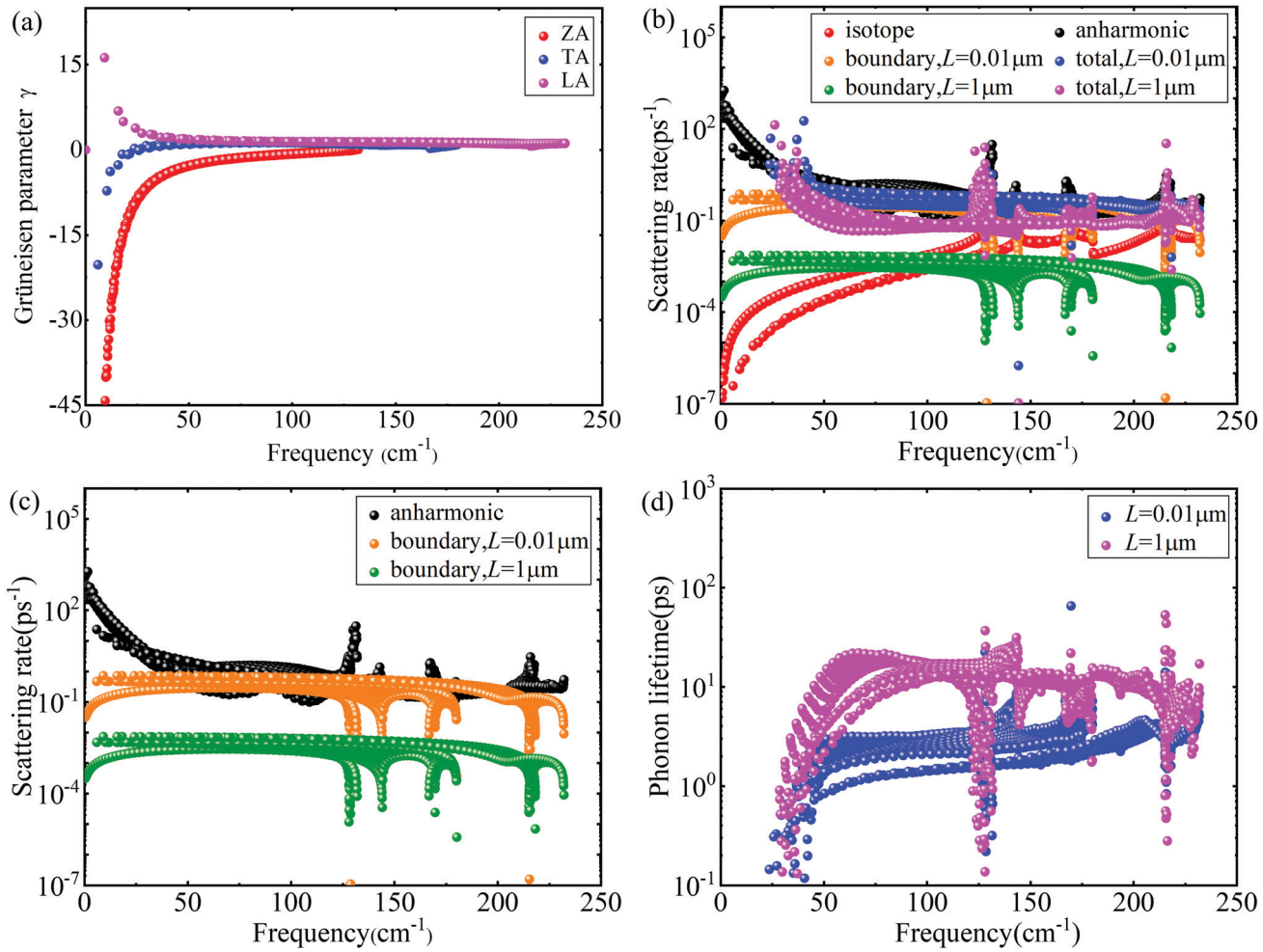

Fig. 5 (a) The Grüneisen parameters of acoustic phonon modes at 300 K. The Grüneisen parameters of acoustic phonon branches (ZA, TA and LA) are indicated in red, blue and magenta, respectively. (b) Acoustic phonon modes scattering rate of different scattering mechanisms for L = 0.01 μm and 1 μm. The phonon–isotope scattering rate is indicated in red. The anharmonic three phonon scattering rate is indicated in black. The phonon–boundary scattering rate and total scattering rate of L = 0.01 μm and L = 1 μm are indicated in different colors. (c) Acoustic phonon modes scattering rate of anharmonic and boundary scattering mechanisms for L = 0.01 μm and 1 μm. (d) Comparison of phonon lifetime from the acoustic phonon modes for L = 0.01 μm and 1 μm. The phonon lifetime results of L = 0.01 μm and 1 μm are indicated in blue and magenta, respectively.

ZA acoustic branch has the largest γ and strongest anharmonicity in the low-frequency region. The large negative value of γ is mostly attributed to the out-of-plane ZA acoustic phonons shown in Fig. 4(b) and (c). These factors finally lead to a low κ_{lat} of monolayer CSe compared to those of black phosphorene (83.5 W m^{-1} K^{-1}),[34] buckled phosphorene (108.8 W m^{-1} K^{-1}),[17] MoS_2 (84 ± 17 W m^{-1} K^{-1}),[35] and buckled arsenene (65.4 W m^{-1} K^{-1}).[17]

As mentioned above, due to the quantum confinement effect, sample size is more prominent than that of bulk materials. Fig. 5(b) and (c) show the scattering rates of acoustic phonon modes in different mechanisms. We here consider two different sizes including L = 0.01 μm and 1 μm. It is found that three-phonon anharmonic scattering rates are much larger than the situations of the isotope effect and boundary effect. Hence, the anharmonic scattering dominates the overall scattering rates of monolayer CSe. In the low-frequency region, the anharmonic phonon scattering rates decrease rapidly, while boundary scattering rate increases gradually as a function of phonon frequency. When the sample size reduces to 0.01 μm, the boundary scattering rates increase, and follow the trend of the three-phonon anharmonic scattering rates, as shown in Fig. 5(c). However, for L = 1 μm, three-phonon anharmonic scattering is the most important scattering mechanism in a broad frequency. Therefore, the size effect on the lattice thermal conductivity of monolayer CSe should be carefully explored in size-limited nanomaterials. The frequency-dependent phonon relaxation times with different sample sizes are shown in Fig. 5(d). This result of phonon lifetimes consider the phonon–phonon scattering, phonon–isotope scattering, and phonon–boundary scattering. It is found that the phonon lifetimes of acoustic phonon modes increase in the low-frequency region due to the weakened three-phonon anharmonic scattering. At L = 0.01 μm, there is a larger anharmonic phonon scattering and boundary scattering, which lead to small phonon lifetimes. As sample size increases, the role of phonon

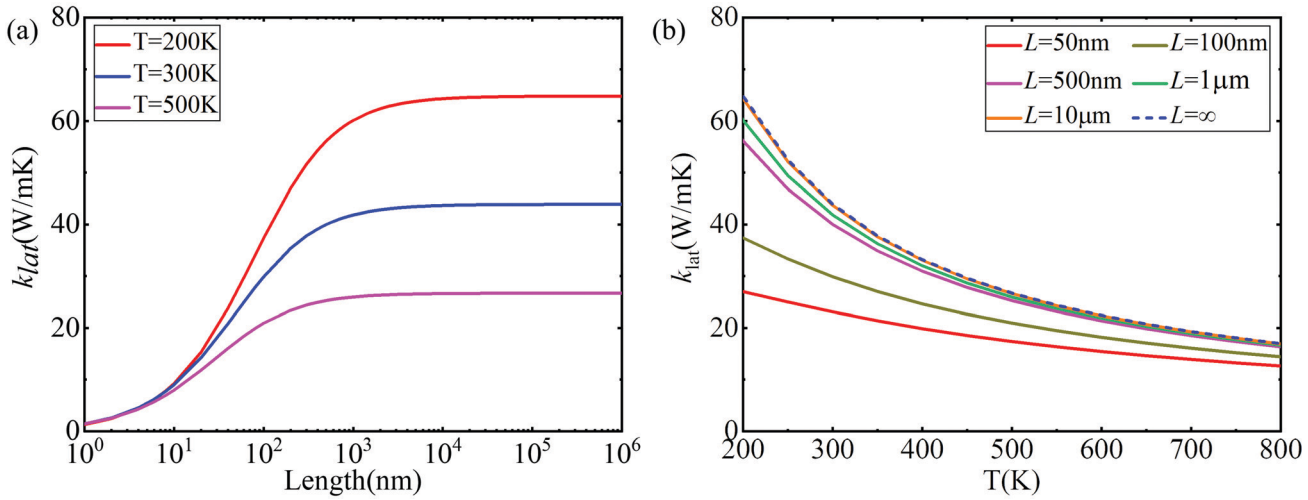

Fig. 6 (a) The κ_{lat} variation as function of sample size for T = 200 K, 300 K and 500 K. (b) The κ_{lat} variation as function of temperature for L = 50 nm, 100 nm, 500 nm, 1 μm, 10 μm and ∞ (L = ∞ refers to the case without phonon–boundary scattering).

boundary scattering gradually decreases. Therefore, the phonon lifetime is considerably increased for L = 1 μm.

In practical application, the electronic devices must have a length scale. The additional phonon–boundary scattering can further affect κ_{lat} significantly the heat transport on the nanoscale and low temperatures. The boundary scattering has been well described and verified in 2D materials.[2,41] The phonon–boundary scattering can be estimated by a empirical formula[6,39,42]

$$\frac{1}{\tau_b} = \frac{|\nu_{vq}|}{L}, \quad (4)$$

where L and ν_{vq} represent the sample size and the averaged phonon group velocity, respectively. Fig. 6(a) shows the κ_{lat} of monolayer CSe as a function of length scale with different temperatures. Due to the increased phonon–boundary scattering effect, the κ_{lat} decreases from 100 nm to 10 nm. Furthermore, κ_{lat} shows an exponential function $\kappa_{lat} \propto \log L$, which has been experimentally verified in graphene and other 2D materials.[43] As L decreases from 1 μm to 10 nm, κ_{lat} decreases from 42 W m^{-1} K^{-1} to 9 W m^{-1} K^{-1} at 300 K, whereas the κ_{lat} decreases by 1.04 times when the L decreases from 10 μm to 1 μm. It is clearly found that boundary scattering limit is achieved at L = 10 μm. Similar characteristics can also be seen at 200 K and 500 K. For example, Specifically, κ_{lat} decreases rapidly at low temperatures since it is more significantly affected by phonon–boundary scattering at low temperatures. Furthermore, the κ_{lat} at different temperatures are almost the same for small sample sizes, which implies a dominant role of phonon–boundary scattering in determining the κ_{lat} of monolayer CSe.

κ_{lat} as a function of sample sizes of monolayer CSe is shown in Fig. 6(b). For comparison, we also plot the κ_{lat} of the infinite size. The κ_{lat} decreases with decreasing sample size owing to the phonon–boundary scattering. It deceases very rapidly with increasing temperature for L = 10 μm, 1 μm, 500 nm and 100 nm. This trend is also verified for the infinite sample size ranging from 200 K to 800 K. For instance, κ_{lat} decreases from 42 W m^{-1} K^{-1} to 29 W m^{-1} K^{-1} at 300 K when L decreases from 10 μm to 100 nm. Our result shows that the κ_{lat} of monolayer CSe can be further decreased by reducing the sample size of nanostructures. Similar behavior is also observed in the lattice thermal conductivity of monolayer penta-silicene and penta-germanene reported by Gao *et al.*[39] and monolayer MoS_2 reported by Zhu *et al.*[42]

3 Conclusion

In summary, we have systematically calculated and explored the heat transport properties of monolayer CSe by first-principles calculations and phonon Boltzmann transport equation. The calculated κ_{lat} is around 42 W m^{-1} K^{-1} at room temperature, which is much lower than that of black phosphorene, buckled phosphorene, MoS_2, and buckled arsenene. The acoustic phonon modes instead of optical phonons contribute the most to the κ_{lat} of monolayer CSe. Furthermore, A + A $\leftrightarrow$ O scattering channels can be significantly suppressed by the large a–o gap, and the LA acoustic phonon branch has a large phonon group velocity and phonon relaxation time. Therefore the LA acoustic phonon branch contributes the most in all phonon modes of monolayer CSe. We also study the phonon–boundary scattering effect on the κ_{lat}. The role of phonon–boundary scattering becomes smaller in a system with a larger size. The size effects of CSe monolayer can persist up to 10 μm at room temperature. Our results also provide a new insight into the size-dependent thermal transport in nanomaterials and guide the design of CSe-based low-dimensional quantum devices, such as thermoelectric devices.

Recently, four phonon scattering have attracted much attention in the heat transport field. One is the phase transition where phonon dispersion at 0 K sometimes shows a negative frequency and can be removed by the finite temperatures.[44] Besides, high thermal conductivity materials have also indicated the crucial role of four phonon scattering.[45,46] Furthermore, unified

first-principles theory can also deal with the four phonon scattering.[47] These developing methods and discoveries deserve more further exploration in the near future.

4 Computational methods

The first-principles calculations are performed using density functional theory as implemented in the VASP code.[48,49] The projector augmented-wave (PAW) pseudopotentials[50] are adopted to describe the interaction between electrons and ions. The exchange–correlation functional of Perdew–Burke–Ernzerhof (PBE)[51] is used. The van der Waals (vdW) correction are described using the zero damping DFT-D3 method of Grimme (zero-damping).[52] During the structure relaxation, a $15 \times 15 \times 1$ Monkhorst–Pack grid is used with an energy cutoff of 500 eV and an energy convergence threshold of 10^{-4} eV. The structures were allowed to relax until the forces on each atom were less than 10^{-4} eV Å^{-1}. A vacuum of 20 Å between monolayer planes along the z-axis was used to avoid spurious interactions between periodic images.

After structure relaxation, the lattice thermal conductivity is obtained by solving the phonon Boltzmann transport equation using the ShengBTE package,[32] which requires the second-order harmonic and third-order force constants (IFCs). The harmonic IFCs were calculated in the Phonopy package[30] with a $7 \times 7 \times 1$ supercell. Anharmonic IFCs were extracted in ShengBTE using a $5 \times 5 \times 1$ supercell. In order to get the converged κ_{lat} value, the interaction cutoff is the up to tenth-nearest-neighbor atoms. Fig. S1 and S2 (ESI†) show the convergence tests of κ_{lat} with different q-grids and scale broadening parameters at 300 K. In compliance with this convergence trend, the q-grid of $250 \times 250 \times 1$ and $200 \times 200 \times 1$ are employed to RTA and iterative solution, respectively. A scale broadening parameter of 1.0 for the Gaussian smearing is used to obtain a converged κ_{lat}. Taking into account long-range electrostatic interactions, the Born effective charges and the dielectric constants are calculated, which were added to the dynamical matrix as a correction.

Conflicts of interest

There are no conflicts to declare.

Acknowledgements

We thank Kunpeng Yuan for helpful discussions. This work is supported by the National Natural Science Foundation of China (Grant No. 61564002 and 11664005), the International Scientific and Technological Cooperation Projects of Guizhou Province, China (Grant No. [2013]7019), the Scientific and Technological Projects of Guizhou Province, China (Grant No. [2010]2146), the Key Laboratory of Low Dimensional Condensed Matter Physics of Higher Educational, Institution of Guizhou Province, (Grant No. [2016]002). Z. Gao acknowledges the financial support from the MOE tier 1 funding of Singapore (Grant No. R-144-000-402-114).

References

1 Q. Zhang, Y. Feng, X. Chen, W. Zhang, L. Wu and Y. Wang, *Nanomaterials*, 2019, **9**, 598.
2 A. A. Balandin, S. Ghosh, W. Bao, I. Calizo, D. Teweldebrhan, F. Miao and C. N. Lau, *Nano Lett.*, 2008, **8**, 902–907.
3 S. Berber, Y.-K. Kwon and D. Tománek, *Phys. Rev. Lett.*, 2000, **84**, 4613.
4 Z. Gao, F. Tao and J. Ren, *Nanoscale*, 2018, **10**, 12997–13003.
5 G. Liu, Z. Gao, G.-L. Li and H. Wang, *J. Appl. Phys.*, 2020, **127**, 065103.
6 Z. Rashid, A. S. Nissimagoudar and W. Li, *Phys. Chem. Chem. Phys.*, 2019, **21**, 5679–5688.
7 T. Hori and J. Shiomi, *Sci. Technol. Adv. Mater.*, 2019, **20**, 10–25.
8 B. Xu, Q. Xia, J. Zhang, S. Ma, Y. Wang, Q. Xu, J. Li and Y. Wang, *Comput. Mater. Sci.*, 2020, **177**, 109588.
9 L.-D. Zhao, S.-H. Lo, Y. Zhang, H. Sun, G. Tan, C. Uher, C. Wolverton, V. P. Dravid and M. G. Kanatzidis, *Nature*, 2014, **508**, 373–377.
10 Z. Gao and J.-S. Wang, *ACS Appl. Mater. Interfaces*, 2020, **12**, 14298–14307.
11 Z. Zhu and D. Tománek, *Phys. Rev. Lett.*, 2014, **112**, 176802.
12 J. L. Zhang, S. Zhao, C. Han, Z. Wang, S. Zhong, S. Sun, R. Guo, X. Zhou, C. D. Gu, K. D. Yuan, Z. Li and W. Chen, *Nano Lett.*, 2016, **16**, 4903–4908.
13 Y. Zhou, M. Zhao, Z. W. Chen, X. M. Shi and Q. Jiang, *Phys. Chem. Chem. Phys.*, 2018, **20**, 30290–30296.
14 H. Jiang, T. Zhao, Y. Ren, R. Zhang and M. Wu, *Sci. Bull.*, 2017, **62**, 572–578.
15 S. S. Batsanov, *Inorg. Mater. (Transl. of Neorg. Mater.)*, 2001, **37**, 871–885.
16 Z. Gao, X. Dong, N. Li and J. Ren, *Nano Lett.*, 2017, **17**, 772–777.
17 G. Zheng, Y. Jia, S. Gao and S.-H. Ke, *Phys. Rev. B*, 2016, **94**, 155448.
18 Q. Zhang, T. Xin, X. Lu and Y. Wang, *Materials*, 2018, **11**, 431.
19 Z.-Y. Hu, K.-Y. Li, Y. Lu, Y. Huang and X.-H. Shao, *Nanoscale*, 2017, **9**, 16093–16100.
20 B. Peng, H. Zhang, H. Shao, Y. Xu, G. Ni, R. Zhang and H. Zhu, *Phys. Rev. B*, 2016, **94**, 245420.
21 B. Peng, D. Zhang, H. Zhang, H. Shao, G. Ni, Y. Zhu and H. Zhu, *Nanoscale*, 2017, **9**, 7397–7407.
22 P.-F. Liu, T. Bo, J. Xu, W. Yin, J. Zhang, F. Wang, O. Eriksson and B.-T. Wang, *Phys. Rev. B*, 2018, **98**, 235426.
23 A. Taheri, C. Da Silva and C. H. Amon, *Phys. Rev. B*, 2019, **99**, 235425.
24 K. Yuan, X. Zhang, L. Li and D. Tang, *Phys. Chem. Chem. Phys.*, 2019, **21**, 468–477.
25 T. K. Gajaria, S. D. Dabhi and P. K. Jha, *Sci. Rep.*, 2019, **9**, 1–20.

26 H. L. Kagdada, P. K. Jha, P. Śpiewak and K. J. Kurzydłowski, *Phys. Rev. B*, 2018, **97**, 134105.
27 H. L. Kagdada, P. K. Jha, P. Śpiewak and K. J. Kurzydłowski, *J. Appl. Phys.*, 2018, **124**, 235701.
28 H. Xiao, W. Cao, T. Ouyang, S. Guo, C. He and J. Zhong, *Sci. Rep.*, 2017, **7**, 45986.
29 L. Lindsay, D. A. Broido and T. L. Reinecke, *Phys. Rev. Lett.*, 2013, **111**, 025901.
30 A. Togo and I. Tanaka, *Scr. Mater.*, 2015, **108**, 1–5.
31 L. F. Huang, P. L. Gong and Z. Zeng, *Phys. Rev. B: Condens. Matter Mater. Phys.*, 2014, **90**, 045409.
32 W. Li, J. Carrete, N. A. Katcho and N. Mingo, *Comput. Phys. Commun.*, 2014, **185**, 1747–1758.
33 P. Torres, F. X. Alvarez, X. Cartoixà and R. Rurali, *2D Mater.*, 2019, **6**, 035002.
34 L. Zhu, G. Zhang and B. Li, *Phys. Rev. B: Condens. Matter Mater. Phys.*, 2014, **90**, 214302.
35 X. Zhang, D. Sun, Y. Li, G.-H. Lee, X. Cui, D. Chenet, Y. You, T. F. Heinz and J. C. Hone, *ACS Appl. Mater. Interfaces*, 2015, **7**, 25923–25929.
36 X. Gu and R. Yang, *Appl. Phys. Lett.*, 2014, **105**, 131903.
37 X. Gu and R. Yang, *J. Appl. Phys.*, 2015, **117**, 025102.
38 G. A. Slack, *Solid State Physics*, Elsevier, 1979, vol. 34, pp. 1–71.
39 Z. Gao, Z. Zhang, G. Liu and J.-S. Wang, *Phys. Chem. Chem. Phys.*, 2019, **21**, 26033–26040.
40 X. Wu, V. Varshney, J. Lee, T. Zhang, J. L. Wohlwend, A. K. Roy and T. Luo, *Nano Lett.*, 2016, **16**, 3925–3935.
41 D. Nika, E. Pokatilov, A. Askerov and A. Balandin, *Phys. Rev. B: Condens. Matter Mater. Phys.*, 2009, **79**, 155413.
42 L. Zhu, T. Zhang, Z. Sun, J. Li, G. Chen and S. A. Yang, *Nanotechnology*, 2015, **26**, 465707.
43 X. Xu, L. F. Pereira, Y. Wang, J. Wu, K. Zhang, X. Zhao, S. Bae, C. T. Bui, R. Xie, J. T. Thong, B. H. Hong, K. P. Loh, D. Donadio, B. Li and B. Özyilmaz, *Nat. Commun.*, 2014, **5**, 1–6.
44 T. Tadano and S. Tsuneyuki, *Phys. Rev. B: Condens. Matter Mater. Phys.*, 2015, **92**, 054301.
45 J. S. Kang, M. Li, H. Wu, H. Nguyen and Y. Hu, *Science*, 2018, **361**, 575–578.
46 K. Chen, B. Song, N. K. Ravichandran, Q. Zheng, X. Chen, H. Lee, H. Sun, S. Li, G. A. G. U. Gamage and F. Tian, *et al.*, *Science*, 2020, **367**, 555–559.
47 N. K. Ravichandran and D. Broido, *Phys. Rev. B*, 2018, **98**, 085205.
48 G. Kresse and J. Furthmüller, *Phys. Rev. B: Condens. Matter Mater. Phys.*, 1996, **54**, 11169–11186.
49 G. Kresse and J. Furthmüller, *Comput. Mater. Sci.*, 1996, **6**, 15–50.
50 G. Kresse and D. Joubert, *Phys. Rev. B: Condens. Matter Mater. Phys.*, 1999, **59**, 1758.
51 J. P. Perdew, K. Burke and M. Ernzerhof, *Phys. Rev. Lett.*, 1996, **77**, 3865–3868.
52 S. Grimme, J. Antony, S. Ehrlich and H. Krieg, *J. Chem. Phys.*, 2010, **132**, 154104.